

Article

# Stress-Induced Phase Transformation and Its Correlation with Corrosion Properties of Dual-Phase High Carbon Steel

Wilson Handoko \*, Farshid Pahlevani, Rumana Hossain and Veena Sahajwalla

Centre for Sustainable Materials Research and Technology (SMaRT Centre), School of Materials Science and Engineering, UNSW Sydney, Sydney, NSW 2052, Australia

\* Correspondence: w.handoko@unsw.edu.au; Tel.: +61-425-958-088

Received: 21 June 2019; Accepted: 5 July 2019; Published: 9 July 2019



**Abstract:** It is well known that stress-induced phase transformation in dual-phase steel leads to the degradation of bulk corrosion resistance properties. Predicting this behaviour in high carbon steel is imperative for designing this grade of steel for more advanced applications. Dual-phase high carbon steel consists of a martensitic structure with metastable retained austenite which can be transformed to martensite when the required energy is attained, and its usage has increased in the past decade. In this study, insight into the influence of deformed microstructures on corrosion behaviour of dual-phase high carbon steel was investigated. The generation of strain-induced martensite formation (SIMF) by residual stress through plastic deformation, misorientation and substructure formation was comprehensively conducted by EBSD and SEM. Tafel and EIS methods were used to determine corrosion intensity and the effect of corrosion behaviour on hardness properties. As a result of the static compression load, the retained austenite transformed into martensite, which lowered its corrosion rate by 5.79% and increased the dislocation density and the length of high-angle grain boundaries. This study demonstrates that balancing the fraction of the martensite phase in structure and dislocation density, including the length of high-angle grain boundaries, will result in an increase in the corrosion rate in parallel with the applied compression load.

**Keywords:** dual-phase steel; plastic deformation; dislocation; corrosion; retained austenite; martensite; stress-induced phase transformation; compression load; EBSD

## 1. Introduction

Over the last decade, high carbon steel has been progressively utilised in broad ranges of automotive, construction and mining applications [1]. It has acquired extensive attention due to its unique combination of high strength, hardness and wear resistance properties ideal for various manufacturing applications such as mining drills, slurry pumps, ball bearing, high precision die-casting and milling cutters, making them able to sustain extremely abrasive environments [2,3]. Dual-phase high carbon steel has been designed to have dual-phase martensite and a retained austenite microstructure. Upon applying stress on this steel, the retained austenite transforms into martensite, which enhances its mechanical properties [4,5]. Recent studies revealed that retained austenite improved wear-resistance and sudden breakage could be minimised due to its capacity to absorb energy from impacts and loads [6]. By applying stress on steel dislocations, density increases, which can increase the internal energy of microstructures [7]. Additionally, this can also generate strain-induced martensite formation (SIMF), which affects the corrosion performance of steel. Moreover, this generation and movement of dislocation in the structure during applied stress and deformation results in the generation of low-angle grain boundaries which can be transformed to high-angle grain boundaries if deformation continues.

This stored energy in the microstructure results in phase transformation able to decrease the dislocation density and the internal energy of the microstructure but increase the length of grain boundaries as new smaller grains can be formed through residual stress occurring due to inhomogeneous elastic-plastic modification of grain shape. A previous investigation by Nadlene et al. [8] on ferrite-martensite steel showed that a higher volume fraction of martensitic phase on bimodal steel enhanced the corrosion rate as martensite acted as a cathode while ferrite acted as an anode by quantification of corrosion current in the electrochemical test. Changing the volume fraction of two different phases changes the magnitude of this cathodic and anodic reaction between the two phases and affects the corrosion behaviour of dual-phase steel.

Recent studies by Handoko et al. [9] on dual-phase high carbon steel revealed that a preferential attack on retained austenite was followed by martensite in the corrosion process. This phenomenon was due to the different carbon content in which the martensitic phase possessed a higher percentage as compared to the austenitic phase [9,10]. Other aspects that influenced this behaviour were the dependency of the different size, shape and volume fraction of the retained austenite, where blocky and lengthy grain size led to the decline of grain boundary density and decreased the dissolution of iron atom movement to trigger a corrosion reaction, thus a decline in grain boundary corrosion and enhanced corrosion resistance properties [10]. In mining environments, water scarcity is one of the primary challenges to obtain a good quality groundwater source for mining activities, as mining areas are located in the countryside, such as in desert climates and high altitudes, where the local water reserve is limited. The utilisation of seawater or desalinated water is preferable in such conditions to continue the mining operation and development [11].

This solid-state phase transformation influences the ductility, hardness and wear resistance of high carbon steel [4,5], but its effect on the corrosion behaviour of high carbon steel is an open question. This research aims to understand the effect of stress-induced phase transformation on the corrosion behaviour of dual-phase high carbon steel in an NaCl solution to mimic the use of seawater in mining conditions. The effect of the microstructure of high carbon steel and its processing history are vital to understanding and forecasting its corrosion behaviour, as well as controlling the optimum volume fraction and stability of the austenite phase, which is crucial in designing the prerequisites of its next applications.

## 2. Materials and Methods

Dual-phase high carbon steel with constituent phases of face-centred cubic (fcc)—retained austenite and body-centred cubic (bcc)—martensite structures, consisting of 1.00 C, 0.98 Mn, 0.60 Cr and 0.20 Si (in wt.%) was used in this study. Compression deformation tests on bulk samples were employed at room temperature with a crosshead speed of 0.1 mm/min, a loading pressure of 2.0 GPa and 3.5 GPa using an Instron 8510. Samples were slowly cut at 0.1 mm/s using a Struers Accutom-50 to avoid shear stress and heat transfer, which can initiate the transformation of the phases. All the samples were mounted with a Struers ProntoPress-20, grinded with silicon carbide paper up to 4000 grits using a TegraPol-21, and polished with a diamond suspension of up to 1  $\mu\text{m}$  using a TegraPol-15. The weight of each sample was measured using a Mettler Toledo XS205-DualRange. An amount of 1.0 M NaCl solution was prepared and all samples were immersed in the solution for 60 min and 120 min at room temperature. Then, samples were cleaned using a Unisonics ultrasonic cleaner to remove any corrosion products and dried using a Struers Drybox-2.

High-resolution backscattered electron-based orientation microscopy (EBSD) investigations of the samples were conducted using an Oxford system with an attached Carl Zeiss AURIGA<sup>®</sup> CrossBeam<sup>®</sup> field emission gun scanning electron microscopy (FEG SEM) workstation. Orientation Imaging Microscopy (OIM) analysis version 8 was used to present a number of Kikuchi bands subsequently from Hough transform, and was performed to determine grain boundaries, phase and substructure transformation. Misorientation from grain to grain was exhibited as Kernel Average Misorientation (KAM). The percentage of each phase, martensite and retained austenite for the used samples in this

study was measured using XRD quantitative analysis and reported in a previous study [4]. Other surface morphology imaging was conducted with an SEM Hitachi S-3400X with the accelerating voltage at 15 keV for the samples before (but after slight etching) and after the corrosion test. The electrochemical studies were conducted using a Versatile Multipotentiostat VSP-300 supported by EC-Lab v.11.02 software. This instrument was Hg/HgCl<sub>2</sub> connected to a flat cell equipped with double walls and three different electrodes: the saturated calomel electrode (SCE) as the reference, the platinum electrode as the counter electrode and the high carbon steel sample as the working electrode. For Tafel polarisation quantitative data, an open circuit potential (OCP) system with an immersion of up to 2 h was recorded as the corrosion potential,  $E_{\text{corr}}$ . The exposed surface area of the tested steel sample to electrolyte (3.5 wt% NaCl solution) was 1 cm<sup>2</sup>. Tafel plots were obtained and processed from –250 to 250 mV at a scan rate of 0.5 mV/s. An electrochemical Impedance Spectroscopy (EIS) measurement with an OCP system was carried out at the corrosion potential (10 mV) between the frequency ranges of 100 kHz and 0.01 Hz in the time span of 24 h. The impedance curves were represented in a Nyquist graph. Hardness measurement was conducted prior to the corrosion test and afterwards using a Struers DuraScan Hardness equipped with the Vickers hardness method at a load of 1 HV at least five times to achieve the average hardness value, as per standard procedure of ASTM E-140.

### 3. Results and Discussions

Applying residual stress in this low stacking-fault energy fcc structure steel leads to dislocation pileups [12], crystallographic microbands [13] and strain-induced martensite formation (SIMF) [14,15]. To understand the effect of compressive deformation and stress-induced transformation on this type of steel, an investigation of the transformed microstructure from metastable retained austenite to the martensite phase was conducted before corrosion tests to show the post-deformation microstructural development using EBSD analysis, as shown in Figure 1. The data above 0.12 confidence index (CI) were employed for further analysis. It can be noted that acquired data above 0.12 CI show more than 94% accuracy. EBSD data cleanup was completed by a grain CI Standardisation routine, and then a CI > 0.1 partition was created to evaluate the data quality. This approach did not change any of the measured orientations, which is very important for the microstructural characterisation. Additionally, during post processing, the software sorted these orientations by ranking them using voting scheme  $CI = (V_a - V_b)/V_{\text{ideal}}$ , where a and b refer to the number of votes on the first and second orientations and “ideal” is defined as the total number of votes from the identified bands. Such grain size and misorientation quantitative data can be effectively utilised for characterising in-grain misorientation development and deformation-induced grain fragmentation in deformed steel [16]. The EBSD micrograph of base-material showed the presence of retained austenite with martensite, which contained a substantial fraction of ~55% of retained austenite. After the compression-retained austenite transformed to the martensite phase, its percentage reduced to ~35% at 2.0 GPa and ~20% at 3.5 GPa [4]. Kernel Average Misorientation (KAM) analysis was utilised to predict local misorientation surrounding a measurement area of the samples, as presented in Figure 1b, where dislocation density is relatively low in the base-material. KAM provides additional information on lattice distortions and deformation localisations. From the EBSD data, KAM can be obtained from the average misorientation around a measurement point in relation to a defined set of the nearest neighbouring points. Therefore, a high KAM value indicates high dislocation density. In this analysis, neighbouring pixels with a misorientation angle lower than a threshold of 5° were taken to exclude other boundaries (e.g., grain boundary, special feature boundary, etc). Increasing the compression load misorientation close to the martensite and austenite grain boundaries exhibited a shift in the distribution toward higher local misorientation.

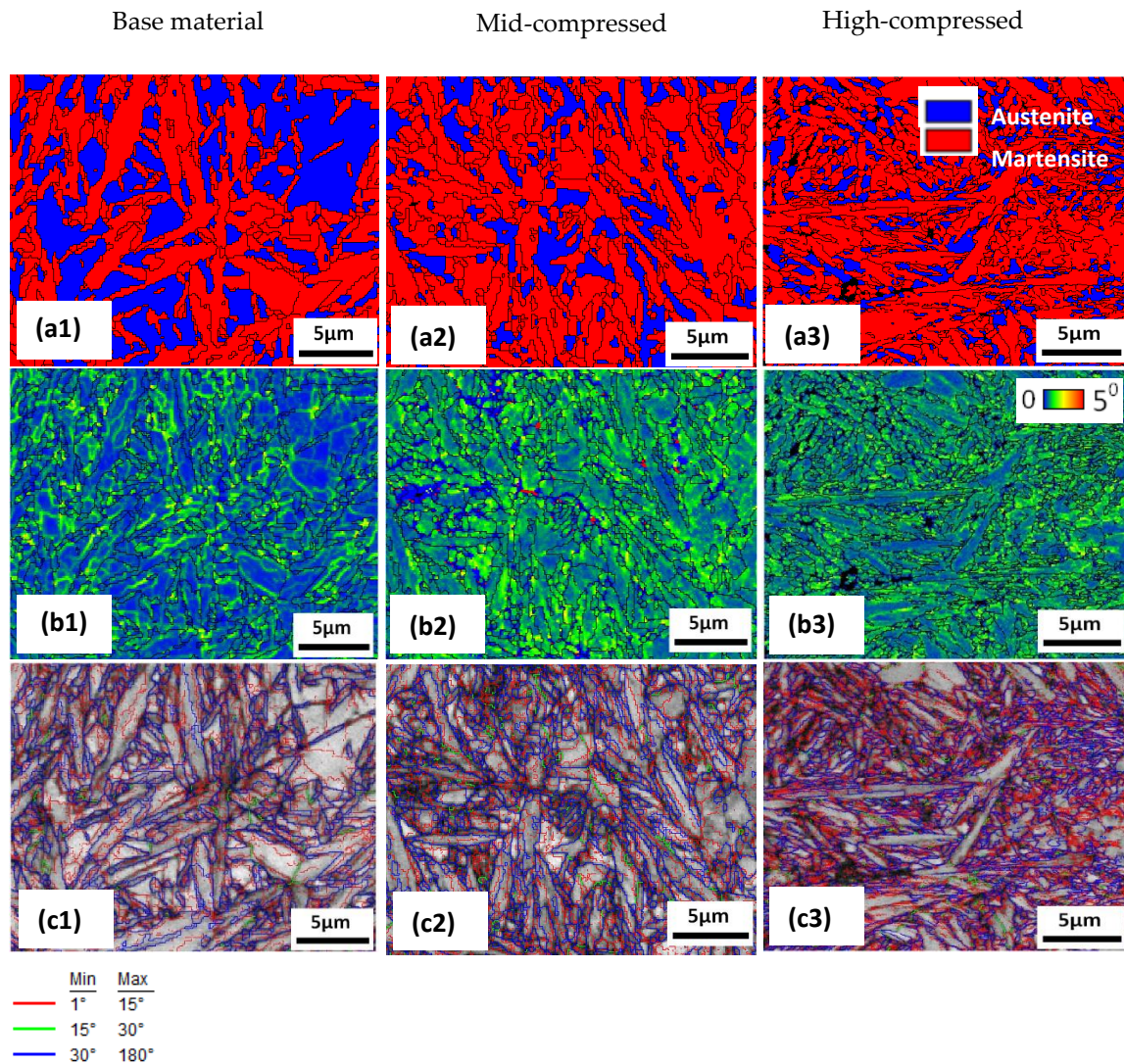


**Figure 1.** EBSD micrograph of the initial material before and after compression tests at different compression forces (a) Phase map; red is the martensite and blue is the retained austenite. Black lines are grain boundaries with a misorientation angle of more than 15° in the phase map (b) Kernel Average Misorientation (KAM) map; mapping is shown from 1° to 5° misorientation and (c) Grain boundary mapping; red line is for grain boundaries up to 15°, green line is for 15° to 30° and blue line is for more than 30°.

Due to compressive deformation, the misorientation angle inclined and when this angle reached 15°, a new grain boundary was created, so the KAM value decreased slightly on the map (comparing Figure 1b2,b3, the KAM value reduced for a while as new grains formed due to deformation). This formation of the new grains can be confirmed by Figure 1a, which shows smaller grain size in the high-compressed sample, as plastic deformation decreased the average grain size value. Overall, at different levels of plastic deformation, the strain localisation was differentiated from EBSD imaging with new lattice curvatures inside previously deformed grain microstructures. With the increasing compressive load, the residual stress and the formation of new grains, the length of the high-angle grain boundaries increased, as seen in Figure 1c. The length of the grain boundaries for these three samples was calculated in different ranges, summarised in Figure 2.

Unlike the formation of dislocated substructures, the deformation in dual-phase steel can lead to the generation of strain-induced martensite [17]. Strain-localised areas possessed higher misorientation, as SIMF was observed on parts of these areas. This martensitic phase was predicted to nucleate on these

localisations and SIMF corresponded with the deterioration of corrosion resistance properties [18–20]. From these EBSD micrographs, it can be summarised that the lengths of low-angle and high-angle grain boundaries were increased by applying compression loads. A previous study demonstrated that this led to an increasing corrosion rate intensity and susceptibility to grain boundary corrosion on, along and within the boundaries [21] but at the same time, the percentage of martensite increased, which decreased the corrosion rate [22]. Corrosion tests and further surface topographical imaging analysis were required to understand the effect of this solid-phase transformation on corrosion behaviour. Microstructural analysis by SEM was conducted before and after the corrosion tests to analyse how different grain boundary shapes, sizes and volume fractions of the martensite and austenite phases affected corrosion behaviour in the NaCl solution, as exhibited in Figure 3. It can be observed that by increasing the compression load, the corrosion rate and the changes in the microstructure increased, especially in conjunction with the different grains and the areas where the concentration of the grain boundaries was increased. These areas are marked with circles in Figure 3, which assist in tracking changes in the microstructure during corrosion. The base-material remained almost unchanged after 60 min and little alteration on the austenite phase occurred after 120 min.

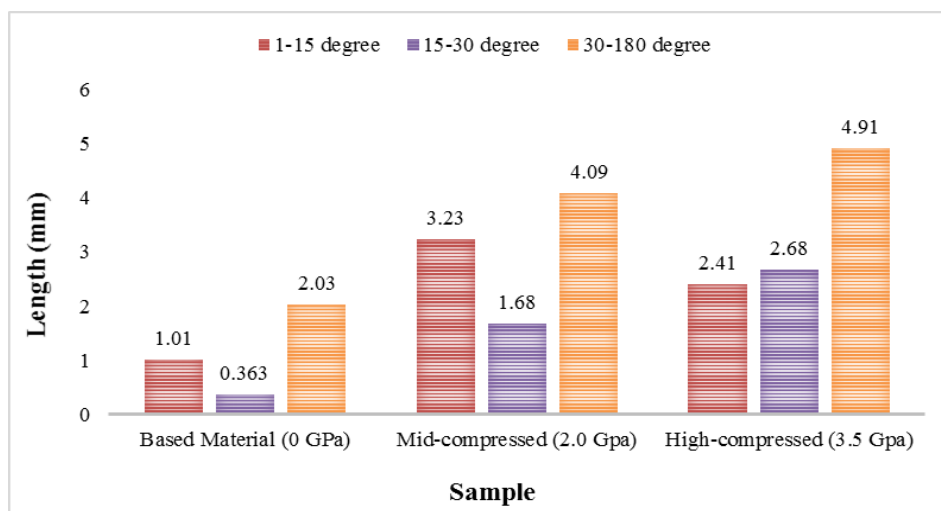


**Figure 2.** Length of the boundaries according to the rotation angle for dual-phase high carbon steels.

For the mid-compressed sample, degradation of the austenite started after 60 min, and more deterioration during this phase as well as the martensitic phase happened at 120 min of corrosion. As misorientation and dislocation density increased as compared to the base-material and new grains were formed during the solid-state transformation by the residual stress, this led to the risk of high-level grain boundary corrosion. Furthermore, on the highest deformed steel sample, severe damage on the austenite and moderate damage on the martensite can be observed at 60 min into the corrosion attack, and more corrosion after 120 min of immersion in the corrosive solution. The formation of a smaller martensitic phase increased the length of grain boundaries in the structure, as summarised in Figure 2, which indicated a had higher potential for grain boundary corrosion to occur. More pointedly, the bulk analysis overwhelmingly demonstrated that the deformation attributing to SIMF predominantly decreased the corrosion resistance [23,24].

Microstructural analysis using SEM showed that the corrosion resistance properties of dual-phase high carbon steel were dependent on the grain size, shape and distribution of SIMF. The sub-micron grain structure, dislocation pile-ups and the existence of SIMF can be attributed to the acceleration of pitting corrosion initiation [25,26]. This is because the different grades of steel substrate influenced its passive films and SIMF and were stipulated to act as “defective oxides” [27]. From SEM, deformation played a more dominant role in the effect of corrosion behaviour than in the solid-state transformation from austenite into martensite, as the highest deformed steel possessed the most severe damage.

Afterwards, the microstructure and the corrosion behaviour of the samples were investigated, and all the important parameters that affected the corrosion behaviour of the high carbon steel during the stress-induced phase transformation are summarised in Figure 4. The experimental results show that the stress-induced phase transformation of austenite to martensite by static compressive load increased the martensite phase, which increased the corrosion resistance. At the same time, this increased the dislocation density and misorientation during deformation. This also increased the length of the high-angle grain boundaries and reduced the average grain size. The combination of all these measures led to an increased corrosion rate.

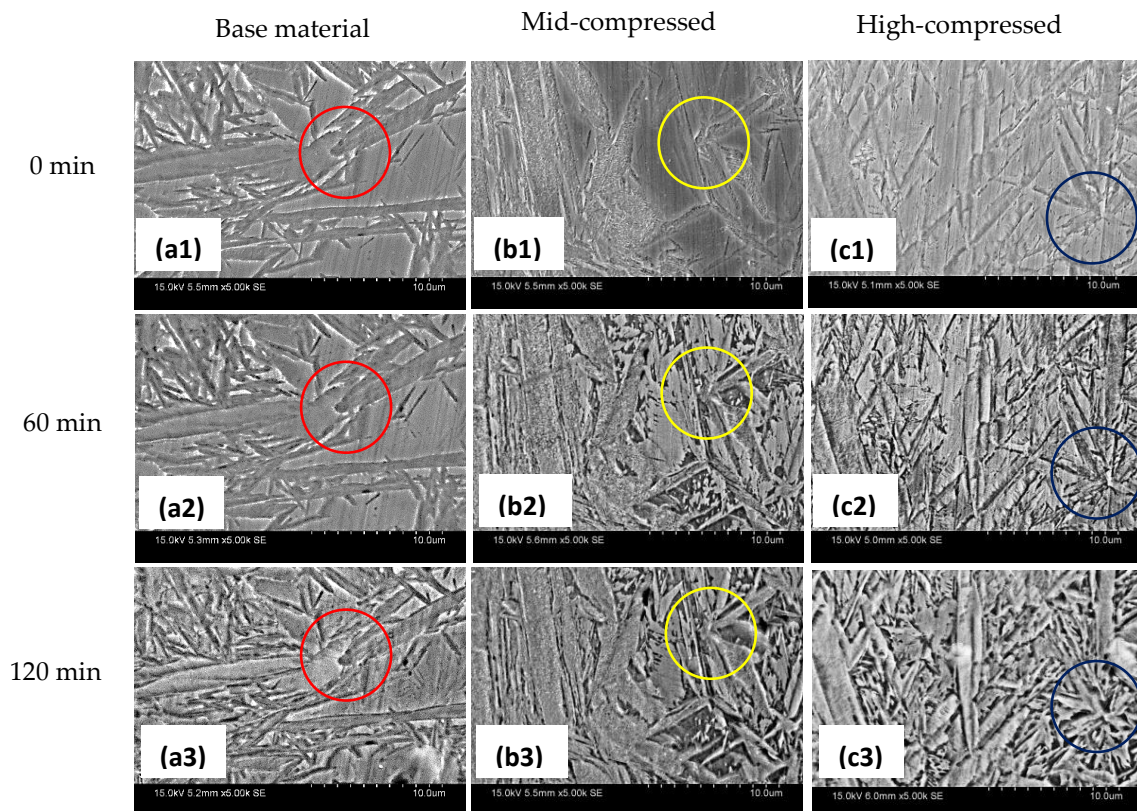


**Figure 3.** The SEM images of three different samples before and after corrosion, where (a) shows base-material, (b) shows a mid-compressed sample, and (c) shows a high-compressed sample; (a1), (a2) and (a3) are images of samples before corrosion; (b1), (b2) and (b3) are images of samples after 60 min into 1.0 M NaCl solution; (c1), (c2) and (c3) are images of samples after 120 min in 1.0 M NaCl solution.

After the microstructural analysis, the precise measurement of the electrochemical tests was conducted to generate potentiodynamic polarisation and Nyquist curves, which can be used to predict different corrosion rates. On the Tafel plot, the overall current density results of the oxidation and reduction reached equilibrium at cross point on an anodic slope (top-sided curve) for a steel dissolution chemical reaction and a cathodic slope (bottom-sided curve) for a hydrogen transformation reaction. The parameters of interest are presented schematically in Figure 5. Tafel polarisation curves were generated, demonstrating that by increasing the compression load, the corrosion rate increased. Plastic deformation played a major role in inclining the corrosion intensity as movement of ions within the corrosion products continuously escalated, thus increasing the number of dislocations [28,29]. More deformations occurred on and along the grain boundary, and both martensitic and austenitic phases became more susceptible to grain boundary corrosion as volume expansion generated plastic strain and residual stress along the adjacent line between the interfaces [30].

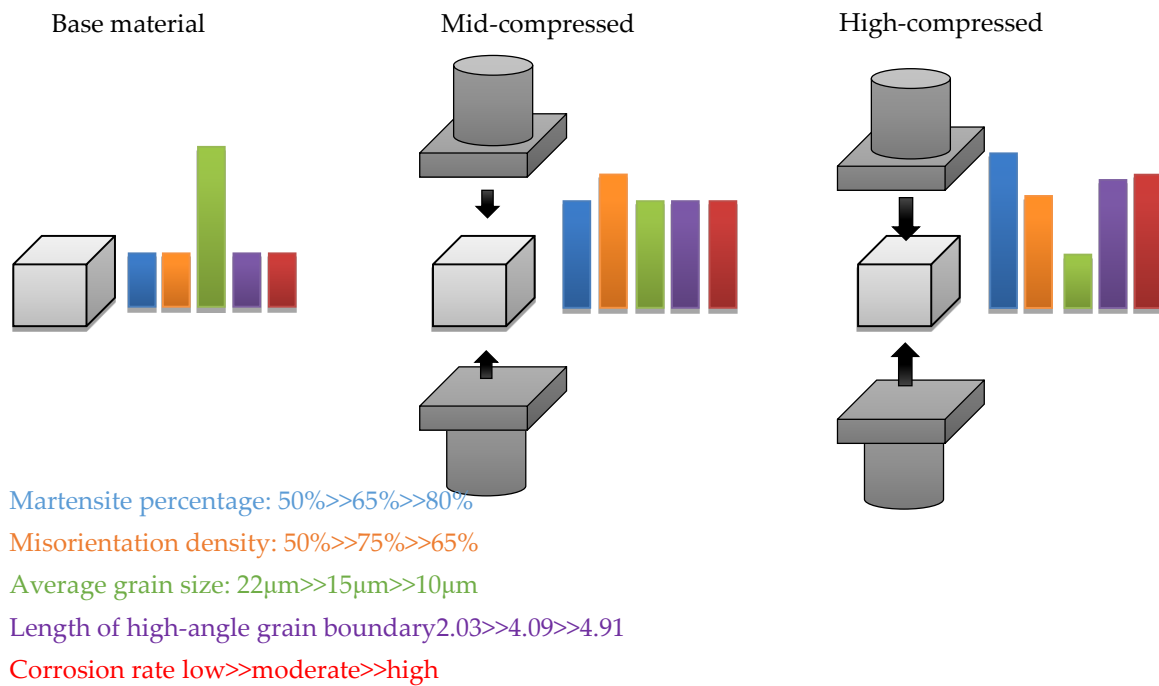


**Figure 4.** Schematic illustration of the effect of stress-induced phase transformation on martensitic percentage, misorientation density, average grain size, length of grain boundary and overall corrosion rate.

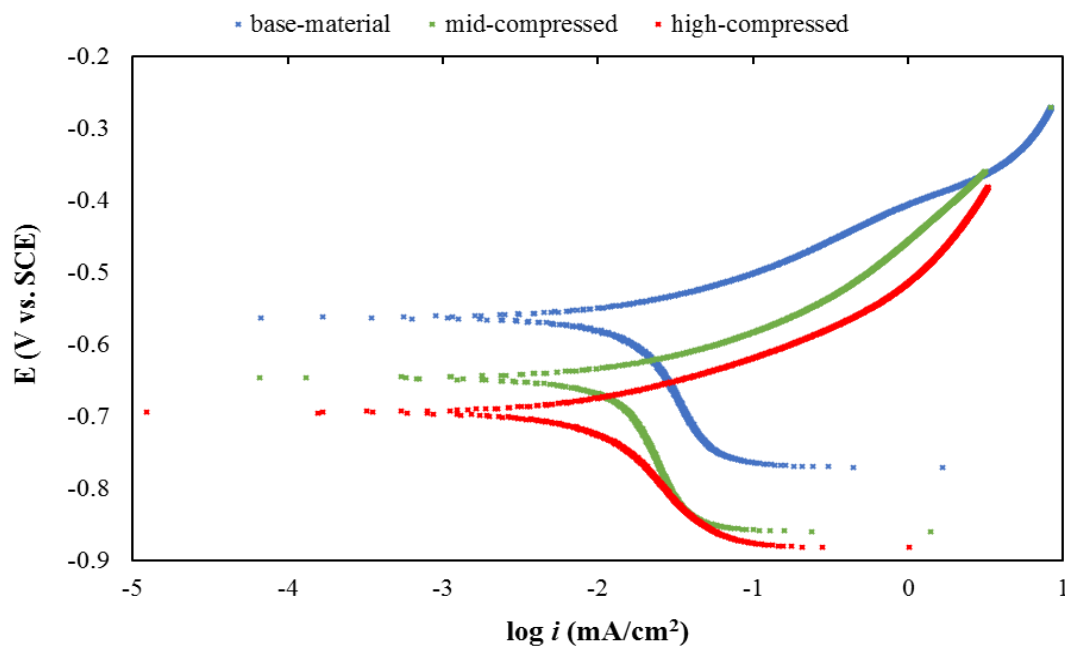


**Figure 5.** The Tafel polarisation curves for high carbon steel samples in 1.0 M NaCl solution.

The acquired quantitative data were processed and are summarised in Table 1, in which the different material properties between undeformed and deformed specimens are presented in various corrosion current density  $i_{corr}$  values, where the lower value had better corrosion resistance properties. This indicates that the base-material sample had lower susceptibility towards corrosion damage than both the mid-compressed and high-compressed samples. As indicated,  $i_{corr}$  increased with plastic strain. It can be stated that such modification of the microstructures was predicted to lower its electrochemical properties by around 5.79%, as compared to the base-material sample, due to the plastic deformation correlated to SIMF. The corrosion potential  $E_{corr}$  values on the base-material were 14.9% and 23.3%, more toward the nobler side than the mid-compressed and high-compressed samples.

The inability of dislocation channels to alleviate stress by slip on, along or within the grain boundary, led to a high level of localised stress that contributed to propensity toward the initiation of stress corrosion cracking (SCC) [31,32]. These statistical data demonstrate that the stability or retention of the retained austenite phase depends on the existence of SIMF. This means that the high-compressed steel sample had the lowest retained austenite stability due to its dislocation pileups and higher SIMF presence, which contributed to a higher pitting corrosion.

**Table 1.** Electrochemical data for high carbon steel samples in 1.0 M NaCl solution.

Sample-ID	$E_{corr}$ (mV vs. SCE)	$\log i_{corr}$ (mA/cm <sup>2</sup> )
Base-Material	$-562 \pm 3$	$1.90 \pm 0.05$
Mid-Compressed	$-646 \pm 6$	$1.94 \pm 0.07$
High-Compressed	$-693 \pm 4$	$2.01 \pm 0.03$

Further investigations were conducted using the electrochemical impedance spectroscopy technique to support the findings in the potentiodynamic polarisation curves above. EIS has proven to be a very useful tool to investigate the corrosion processes of steels in various environments. As shown in the measured Nyquist plots in Figure 6, in the presence of less microstructural deformation and low-level of dislocation on the base-material, the inductive loop disappeared more and the size of the high-frequency (HF) loop expanded. This was proven through the increased diameter of the capacitive loop, which exhibited an inclination on the charge-transfer resistance and a reduction of the corrosion current intensity; hence, corrosion resistance properties improved on dual-phase high carbon steel, as a less stress-induced phase transformation occurred. Additionally, impedance curves are in a semi-circle shape at the HF loop, meaning that the charge transfer process through electrolyte mostly dominated the corrosion of the high carbon steel. Therefore, based on the EIS measurement results, plastic deformation on both internal and external steel caused more dislocation density with higher energy internal storage and increased in hardness, thus triggering the enhancement of atomic migration, which led to the promotion of a higher corrosion rate [33,34].

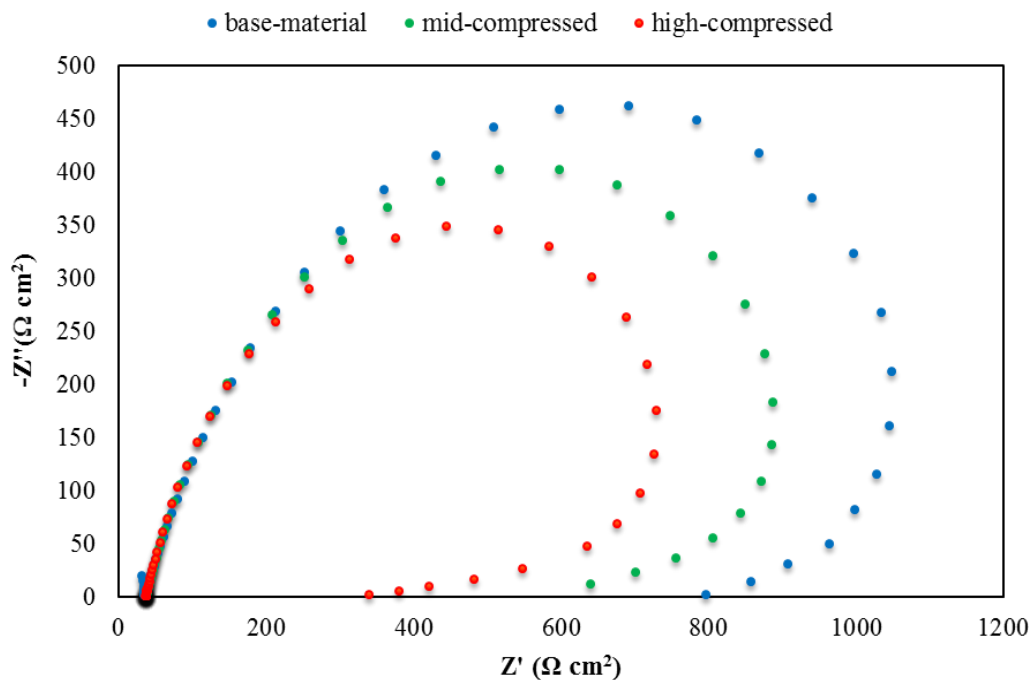


**Figure 6.** The Nyquist plots from EIS data for high carbon steel in 1.0 M NaCl solution.

The approaches shown in this study distinctly illustrate that corrosion rate intensity, acquired by classic electrochemical test methods, can be augmented by various topographical observations in detail for a thorough characterisation of the corrosion resistance properties of dual-phase high carbon steel. Overall corrosion mechanisms in this type of steel were the boundary corrosion and the localised pitting corrosion, as shown in the previous microstructural imaging. This phenomenon was due to localised electrochemical dissolution, as the breakdown of passive film occurred in certain areas of the exposed steel surface, hence, microscopic scale corrosion pits were initiated [35,36]. The influence of compressive deformation led to stress-induced transformation on metastable retained austenite to martensite phase that generated more new grains, grain boundaries, lattice mismatch and dislocation density, thus escalating vulnerability to corrosion attacks, especially on grain boundary corrosion. Deformation produced more dislocations and led to more passive film breakdowns that caused an increase in pit growth on the most deformed microstructures of the steel sample. It was further demonstrated that the mechanical test was carried out on the hardness test to prove more material loss on the deformed sample, as compared to the undeformed sample, as the cause of more pit growth.

Vickers hardness tests were conducted to determine to what extent the compressive deformation can affect the hardness properties as well as the corrosion properties of martensite–austenite high carbon steel. Table 2 summarises the hardness value for each sample before and after corrosion. By increasing the static compression load, the hardness increased because of the solid-state phase transformation of the retained austenite to martensite, at the same time increasing the dislocation density and decreasing the average grain size. However, the decrease in the hardness due to the corrosion attack was slightly different in all the samples. One of the reasons is due to less corrosion in the base material [9,10] compared to the other two samples because of the solid-state phase transformation that increased the dislocation density, plastic deformation and residual stress between the constituent phases. Another reason is that corrosion has a negative effect on surface mechanical properties, such as grain boundary corrosion between the interface of martensite and austenite phases, which weakens the overall integrity of each phase, thus reducing the surface hardness properties.

**Table 2.** The effect of compressive deformation on the hardness properties of the high carbon steel specimen before and after the corrosion test in 1.0 M NaCl solution at various times.

Time (h)	Hardness (HV)		
	Base-Material	Mid-Compressed	High-Compressed
0	792.3 ± 0.4	795.9 ± 0.03	798.4 ± 0.04
1	792.0 ± 0.5	795.7 ± 0.05	798.1 ± 0.04
2	791.6 ± 0.3	795.4 ± 0.06	797.8 ± 0.03

#### 4. Conclusions

The influence of stress-induced phase transformation on the corrosion-resistant properties of martensite–austenite high carbon steel was studied using different microstructural and electrochemical investigations. The post-deformation corrosion resistance properties were then investigated. It was demonstrated that by increasing the compressive stress, the numbers of the new grain, grain boundary, lattice misorientation, dislocation density and anodic-cathodic reaction increased, which resulted in an increased corrosion rate. Direct observation using EBSD showed a clear attribution of localised misorientation to the prevalence of passivity. An increase in the length of high-angle grain boundaries detected through KAM analysis and more SIMF presence through plastic deformation led to more grain boundary corrosion and a higher level of pit growth, which resulted in an increase in the corrosion intensity. A powerful electrochemical analysis proved that the lowest current intensity in the Tafel polarisation curve and the smallest radius in the Nyquist plot appeared on the highest deformed microstructures, meaning that a higher corrosion rate up to 5.78% of high-compressed steel occurred, as compared to the base-material sample. Thus, the notion of dislocation pileups and SIMF existence was correlated to a reduction in the corrosion performance. The increase in pit growth was

due to the increased breakdown of localised passive films on the steel sample with an applied load of 3.5 GPa. Overall, the results show that compressive deformation overwhelmed the influence of solid-state transformation on the retained austenite into the martensite phase, which contrasted its effect to improve the corrosion resistance. It is crucial to identify the effect of stress-induced phase transformation, such as SIMF, on dual-phase high carbon steel, to understand and predict its corrosion behaviour for selecting an appropriate balance parameter between the plastic deformation effect and the volume fraction of each phase to achieve the maximum corrosion-resistant properties without modifying its elemental composition.

**Author Contributions:** W.H. performed experiments and data analysis. F.P. designed the project and experiments and critically analysed the data. R.H. performed EBSD study and data analysis. V.S. supervised the study and gave suggestions to revise the manuscript. W.H. wrote the manuscript and all authors analysed the data, discussed the results, read and approved the final manuscript.

**Funding:** This research was conducted in cooperation with Australian Government Research Training Program (RTP) and Australian Research Council's Industrial Transformation Research Hub funding scheme (project IH130200025). We gratefully acknowledge the technical support provided by the Analytical Centre in UNSW Sydney.

**Conflicts of Interest:** The authors declare no conflicting interests.

## References

- Hui, W.; Zhang, H.; Zhang, Y.; Zhao, X.; Shao, C. Effect of nickel on hydrogen embrittlement behavior of medium-carbon high strength steels. *Mater. Sci. Eng. A* **2016**, *674*, 615–625. [[CrossRef](#)]
- Kwon, K.; Yi, I.; Ha, Y.; Um, K.; Choi, J.; Hono, K.; Oh-ishi, K.; Kim, N. Origin of intergranular fracture in martensitic 8Mn steel at cryogenic temperatures. *Scr. Mater.* **2013**, *69*, 420–423. [[CrossRef](#)]
- Sohn, S.; Song, H.; Jo, M.; Song, T.; Kim, H.; Lee, S. Novel 1.5 GPa-strength with 50%-ductility by transformation-induced plasticity of non-recrystallized austenite in duplex steels. *Sci. Rep.* **2017**, *7*, 1255. [[CrossRef](#)] [[PubMed](#)]
- Hossain, R.; Pahlevani, F.; Sahajwalla, V. Effect of small addition of Cr on stability of retained austenite in high carbon steel. *Mater. Charact.* **2017**, *125*, 114–122. [[CrossRef](#)]
- Hossain, R.; Pahlevani, F.; Quadir, M.; Sahajwalla, V. Stability of retained austenite in high carbon steel under compressive stress: an investigation from macro to nano scale. *Sci. Rep.* **2016**, *6*, 34958. [[CrossRef](#)] [[PubMed](#)]
- Hossain, R.; Pahlevani, F.; Witteveen, E.; Banerjee, A.; Joe, B.; Prusty, B.; Dippenaar, R.; Sahajwalla, V. Hybrid structure of white layer in high carbon steel—Formation mechanism and its properties. *Sci. Rep.* **2017**, *7*, 13288. [[CrossRef](#)] [[PubMed](#)]
- Liang, Z.; Zhao, Q.; Singh, P.M.; Wang, Y.; Li, Y.; Wang, Y. Field studies of steam oxidation behavior of austenitic heat-resistant steel 10Cr18Ni9Cu3NbN. *Eng. Fail. Anal.* **2015**, *53*, 132–137. [[CrossRef](#)]
- Nadlene, R.; Esah, H.; Norliana, S.; Mohd-Irwan, M.A. Study on the Effect of Volume Fraction of Dual Phase Steel to Corrosion Behaviour and Hardness. World Academy of Science, Engineering and Technology. International Journal of Mechanical, Aerospace, Industrial. *Mechatron. Manuf. Eng.* **2011**, *5*, 393–396.
- Handoko, W.; Pahlevani, F.; Sahajwalla, V. Corrosion Behaviour of Dual-Phase High Carbon Steel—Microstructure Influence. *J. Manuf. Mater. Process.* **2017**, *1*, 21. [[CrossRef](#)]
- Handoko, W.; Pahlevani, F.; Sahajwalla, V. The Effect of Low-Quantity Cr Addition on the Corrosion Behaviour of Dual-Phase High Carbon Steel. *Metals* **2018**, *8*, 199. [[CrossRef](#)]
- Kamrunnahar, M.; Urquidi-Macdonald, M. Prediction of corrosion behavior using neural network as a data mining tool. *Corros. Sci.* **2010**, *52*, 669–677. [[CrossRef](#)]
- Zhang, L.; Szpunar, J.; Dong, J.; Ojo, O.; Wang, X. Dependence of Crystallographic Orientation on Pitting Corrosion Behavior of Ni-Fe-Cr Alloy 028. *Metall. Mater. Trans. B* **2018**, *49*, 919–925. [[CrossRef](#)]
- Hernández-Espejel, A.; Domínguez-Crespo, M.; Cabrera-Sierra, R.; Rodríguez-Meneses, C.; Arce-Estrada, E. Investigations of corrosion films formed on API-X52 pipeline steel in acid sour media. *Corros. Sci.* **2010**, *52*, 2258–2267. [[CrossRef](#)]
- Ahmedabadi, P.; Kain, V.; Agrawal, A. Modelling kinetics of strain-induced martensite transformation during plastic deformation of austenitic stainless steel. *Mater. Des.* **2016**, *109*, 466–475. [[CrossRef](#)]

15. Lee, B.; Koizumi, Y.; Matsumoto, H.; Chiba, A. Collective behavior of strain-induced martensitic transformation (SIMT) in biomedical Co–Cr–Mo–N alloy polycrystal: An ex-situ electron backscattering diffraction study. *Mater. Sci. Eng. A* **2014**, *611*, 263–273. [[CrossRef](#)]
16. Srinivasan, N.; Kain, V.; Birbilis, N.; Kumar, B.; Gandhi, M.; Sivaprasad, P.; Chai, G.; Lodh, A.; Ahmedabadi, P.; Samajdar, I. Plastic deformation and corrosion in austenitic stainless steel: A novel approach through microtexture and infrared spectroscopy. *Corros. Sci.* **2016**, *111*, 404–413. [[CrossRef](#)]
17. Rezaee, A.; Kermanpur, A.; Najafizadeh, A.; Moallemi, M.; Samaei Baghbadorani, H. Investigation of cold rolling variables on the formation of strain-induced martensite in 201L stainless steel. *Mater. Des.* **2013**, *46*, 49–53. [[CrossRef](#)]
18. Hong, S.; Kim, M.; Min, D.; Lee, K.; Shim, J.; Kim, D.; Suh, J.; Jung, W.; Choi, I. Unraveling the origin of strain-induced precipitation of M23C6 in the plastically deformed 347 Austenite stainless steel. *Mater. Charact.* **2014**, *94*, 7–13. [[CrossRef](#)]
19. Lv, J.; Luo, H. Effects of strain and strain-induced  $\alpha'$ -martensite on passive films in AISI 304 austenitic stainless steel. *Mater. Sci. Eng. C* **2014**, *34*, 484–490. [[CrossRef](#)]
20. Mirzadeh, H.; Najafizadeh, A. ANN modeling of strain-induced martensite and its applications in metastable austenitic stainless steels. *J. Alloys Compd.* **2009**, *476*, 352–355. [[CrossRef](#)]
21. Murkute, P.; Ramkumar, J.; Choudhary, S.; Mondal, K. Effect of alternate corrosion and wear on the overall degradation of a dual phase and a mild steel. *Wear* **2016**, *368–369*, 368–378. [[CrossRef](#)]
22. Handoko, W.; Pahlevani, F.; Sahajwalla, V. Effect of Retained Austenite Stability in Corrosion Mechanism of Dual Phase High Carbon Steel. World Academy of Science, Engineering and Technology. *Int. J. Mater. Metall. Eng.* **2018**, *12*, 1–5.
23. Zaera, R.; Rodríguez-Martínez, J.; Casado, A.; Fernández-Sáez, J.; Rusinek, A.; Pesci, R. A constitutive model for analyzing martensite formation in austenitic steels deforming at high strain rates. *Int. J. Plast.* **2012**, *29*, 77–101. [[CrossRef](#)]
24. Solomon, N.; Solomon, I. Effect of deformation-induced phase transformation on AISI 316 stainless steel corrosion resistance. *Eng. Fail. Anal.* **2017**, *79*, 865–875. [[CrossRef](#)]
25. Shen, Y.; Li, X.; Sun, X.; Wang, Y.; Zuo, L. Twinning and martensite in a 304 austenitic stainless steel. *Mater. Sci. Eng. A* **2012**, *552*, 514–522. [[CrossRef](#)]
26. Saini, N.; Pandey, C.; Mahapatra, M.M.; Narang, H.K.; Mulik, R.S.; Kumar, P. A comparative study of ductile-brittle transition behavior and fractography of P91 and P92 steel. *Eng. Fail. Anal.* **2017**, *81*, 245–253. [[CrossRef](#)]
27. Misra, R.; Nayak, S.; Mali, S.; Shah, J.; Somani, M.; Karjalainen, L. On the Significance of Nature of Strain-Induced Martensite on Phase-Reversion-Induced Nanograined/Ultrafine-Grained Austenitic Stainless Steel. *Metall. Mater. Trans. A* **2009**, *41*, 3–12. [[CrossRef](#)]
28. Khadraoui, A.; Khelifa, A.; Boutoumi, H.; Mettai, B.; Karzazi, Y.; Hammouti, B. Corrosion Inhibition of Carbon Steel in Hydrochloric Acid Solution by Mentha Pulegium Extract. *Port. Electrochim. Acta* **2014**, *32*, 271–280. [[CrossRef](#)]
29. Ahmad, E.; Karim, F.; Saeed, K.; Manzoor, T.; Zahid, G. Effect of cold rolling and annealing on the grain refinement of low alloy steel. *IOP Conf. Ser. Mater. Sci. Eng.* **2014**, *60*, 1–7. [[CrossRef](#)]
30. Rafiee, E.; Farzam, M.; Golozar, M.; Ashrafi, A. An Investigation on Dislocation Density in Cold-Rolled Copper Using Electrochemical Impedance Spectroscopy. *ISRN Corros.* **2013**, *2013*, 1–6. [[CrossRef](#)]
31. Guo, X.; Chen, K.; Gao, W.; Shen, Z.; Lai, P.; Zhang, L. A research on the corrosion and stress corrosion cracking susceptibility of 316L stainless steel exposed to supercritical water. *Corros. Sci.* **2017**, *127*, 157–167. [[CrossRef](#)]
32. Leskovšek, V.; Godec, M.; Kogej, P. Influence of low-temperature nitriding on the strain-induced martensite and laser-quenched austenite in a magnetic encoder made from 304L stainless steel. *Sci. Rep.* **2016**, *6*, 30979. [[CrossRef](#)]
33. Allam, T.; Abbas, M. Mechanical Properties, Formability, and Corrosion Behavior of Dual Phase Weathering Steels Developed by an Inter-Critical Annealing Treatment. *Steel Res. Int.* **2014**, *86*, 231–240. [[CrossRef](#)]
34. Handoko, W.; Pahlevani, F.; Sahajwalla, V. Enhancing Corrosion Resistance and Hardness Properties of Carbon Steel through Modification of Microstructure. *Materials* **2018**, *11*, 2404. [[CrossRef](#)] [[PubMed](#)]

35. Handoko, W.; Pahlevani, F.; Emmanuelawati, I.; Sahajwalla, V. Transforming automotive waste into TiN and TiC ceramics. *Mater. Lett.* **2016**, *176*, 17–20. [[CrossRef](#)]
36. Burstein, G.; Pistorius, P.; Mattin, S. The nucleation and growth of corrosion pits on stainless steel. *Corros. Sci.* **1993**, *35*, 57–62. [[CrossRef](#)]



© 2019 by the authors. Licensee MDPI, Basel, Switzerland. This article is an open access article distributed under the terms and conditions of the Creative Commons Attribution (CC BY) license (<http://creativecommons.org/licenses/by/4.0/>).